Crack growth in masonry: numerical analysis and sensitivity study for discrete and smeared crack modelling

[1]Leidy Bejarano-Urrego, [1]Els Verstrynge, [2]Giorgia Giardina and [1]Koen Van Balen

[1]Building Materials and Building Technology Division, Civil Engineering Dept. KU Leuven, Kasteelpark Arenberg 40 Box 2448, Heverlee, Belgium

[2]Department of Architecture and Civil Engineering, University of Bath

Corresponding author: leidyelvira.bejaranourrego@kuleuven.be

ABSTRACT

One of the most common obstacles faced by engineers when making numerical models to assess damage in historical masonry lies in defining the most suitable constitutive models when there is shortage of either material characterization or experimental data. This paper presents the implementation of a 2D finite element model (FEM) of a masonry wall by means of two strategies: a discrete cracking meso-model and a continuum smeared cracking macro-model. A sensitivity study is performed to investigate the effect of material properties variation on both modelling strategies, each of which considers the highly non-linear behaviour as well as the brittle cracking of the masonry.

The numerical models are validated through the results obtained from an experimental testing campaign which considered a brick masonry wall subjected to cyclic three-point bending. The results of both modelling strategies compared with experimental results are presented, as well as the criteria considered for material characterization and the sensitivity analysis. Results indicate the suitability of both models to reproduce experimentally observed load capacity, failure mechanism and horizontal deformations. However, the meso-model showed higher accuracy in terms of failure mechanism and plastic deformations. The sensitivity analysis indicated that some material parameters, such as fracture energy, cohesion and tensile strength, significantly govern the final cracking. This is an important criterion for adequately choosing the parameters for further models in which crack width is considered, e.g. for settlement-induced cracking analysis.

KEYWORDS

Numerical analysis, masonry, discrete crack modelling, smeared crack modelling, model calibration, sensitivity study

1. INTRODUCTION

This work investigates the mechanical behaviour of unreinforced brick masonry walls when subjected to differential settlements through discrete and smeared cracking numerical models.

Accumulation of differential settlements may induce various problems to masonry structures, from minor cracks and tilts to large displacements causing distortion or even collapse. Even if a building does not present structural damage, serviceability issues may emerge. Furthermore, differential settlements can increase vulnerability to natural hazards such as earthquakes or flooding [1]. Such settlements are triggered by different factors within building, local and regional scales, including non-uniform building loading, construction of local underground structures and widespread water pumping. To prevent damage propagation, damage levels must be estimated and the effects of settlements mitigated, if necessary. The aim of this paper is to critically analyze modelling strategies for cracking in unreinforced masonry walls under given boundary conditions and vertical loading.

Different analytical and numerical methods to determine settlement-induced building damage have been proposed [2]. One of the most known analytical methods to define the level of damage is the limiting tensile strain method (LTSM), proposed by Burland [3]. This method is based on the assumption that the initiation of visible cracking is related to a critical tensile strain, which lies between 0.05 and 0.1% for unreinforced brick masonry. However, the LTSM presents some drawbacks such as the assumption that the building behaves as a simple linear elastic beam presenting bending and shear deformation, which might be an inaccurate simplification for complex building geometries and brittle materials. On the other hand, numerical models using FEM to model settlement-induced damage have been widely investigated and implemented [2, 4-9]. They are more suitable for complex geometries, describe the material behaviour more accurately by means of non-linear constitutive laws and allow taking into account the soil-structure interaction. Nevertheless, the use of 3D models might be computationally expensive [10] and calibration of model parameters is not straightforward.

This work aims to identify a suitable and accurate numerical modelling approach to quantify settlement-induced damage in unreinforced masonry using discrete cracking and continuum smeared cracking models. Calibration procedures and sensitivity studies were performed to determine reference material property values and to analyse the effect of the variation of these properties on both modelling strategies, for which crack widths, load capacity and failure mechanisms were investigated. A methodology to obtain the material properties for the macro-model in terms of the properties of the meso-model was also elaborated and evaluated on experimental data.

2. EXPERIMENTAL INPUT DATA

Experimental three-point bending tests were performed on a wall in order to induce cracking in a semi-controlled manner (the wall was not notched as the location of the crack was anticipated) and analyse the masonry's non-linear behaviour. Damage progress during the cyclic loading was recorded by monitoring elastic deformations, crack width, deflection and acoustic emissions. To characterize the mechanical properties of the materials, mortar and brick samples as well as couplets were tested under compression and bending. Numerical models were built considering the obtained material properties and validated based on the monitoring results.

2.1 Test setup and monitoring

The tests were performed on a Flemish bond masonry wall of 16 courses in height (960 mm) and 1 unit in thickness (188 mm), as schematically shown in Figure 1. The wall was made of solid clay bricks and 12 mm thick mortar joints, prepared width a hybrid cement-lime mortar. The area between the support points was filled with polyurethane plates to support the specimen's weight and simulate the existence of a compressible soil.

A more detail description of the test setup and monitoring techniques can be found in [10] and [11]. Three cyclic three-point bending tests were performed on the test wall. Each cyclic test consisted of several loading and unloading stages, with increasing peak force for subsequent loading cycles. However, only the monitoring results from the third test, where the failure occurred, are used here for the validation of the numerical models. During this test, a preload of 1kN was applied after which the load was increased at a load rate of 0.333 kN/s until the peak loads of 20, 40 and 60 kN. Following each peak load, the load was decreased up to the selected preload (Figure 2a). The wall failure, identified as an unstable growth of the large macro crack, occurred during the fourth cycle at a load of 76.4 kN. The flexural strength of the masonry member subjected to three-point bending may be calculated from the expression

$$f_{flex} = \frac{3FL}{2WH^2} \quad (1)$$

where F is the peal load, L is the length between supports, W is the cross section width of the sample and H is the height. Applying Expression (1) in the present case, a flexural strength of 1.19 N/mm^2 is obtained.

Results included the crack width measured by means of integrated optical fibres with distributed fibre Bragg grating sensors (FBGs), full-field vertical and horizontal displacement field obtained from stereo-vision digital image correlation (DIC) and vertical displacement at load application point measured with LVDTs.

The highest sensitivity and robustness for deformation and crack monitoring was achieved with the integrated optical fibres with FBGs. The monitored elastic deformation and crack width used for the validation of the numerical model correspond to the data of FBG4 and they are reported below for completeness (Figure 1 and Figure 2b). The obtained strain data were converted into deformation by multiplication with the corresponding base length of 0.8 m, which is the distance between the fibre's anchor points in A and B (see Figure 1). The major crack, which crossed the wall from bottom to top, did not appear in the central position of the wall; this might indicate heterogeneity in material properties, geometry and/or boundary conditions.

Additionally, the full-field vertical and horizontal displacements obtained in the area of interest (AOI) from the stereo-vision digital image correlation (DIC) as well as the vertical displacement at the load application point were also used for validation of the numerical models.

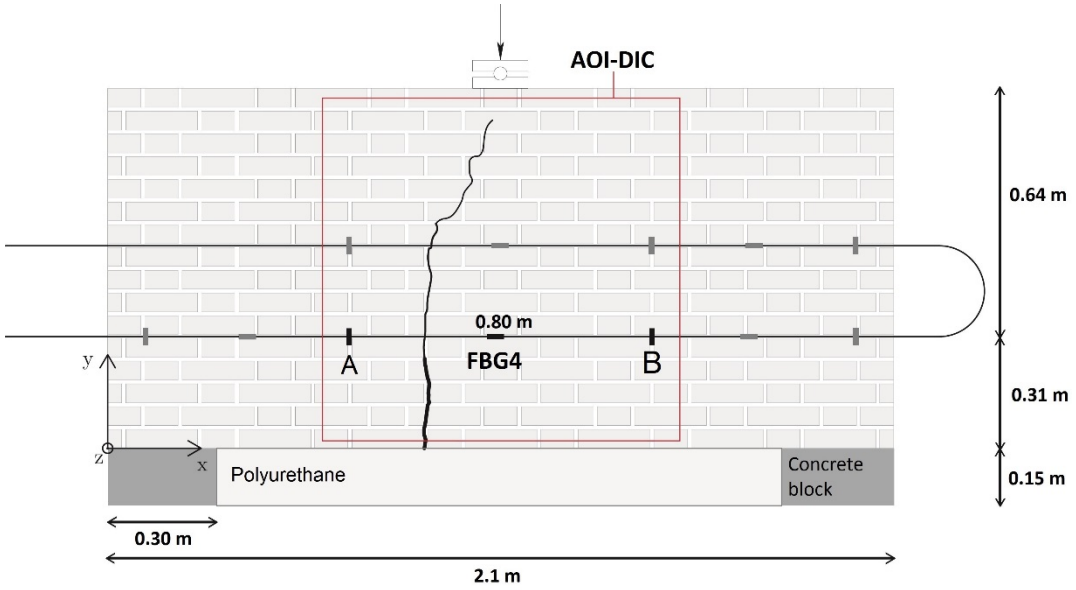

Figure 1. Setup of three-point bending test, fibre Bragg grating sensor (FBG4) and area of interest of Digital Image Correlation (AOI-DIC), with indication of the major crack at the end of the test

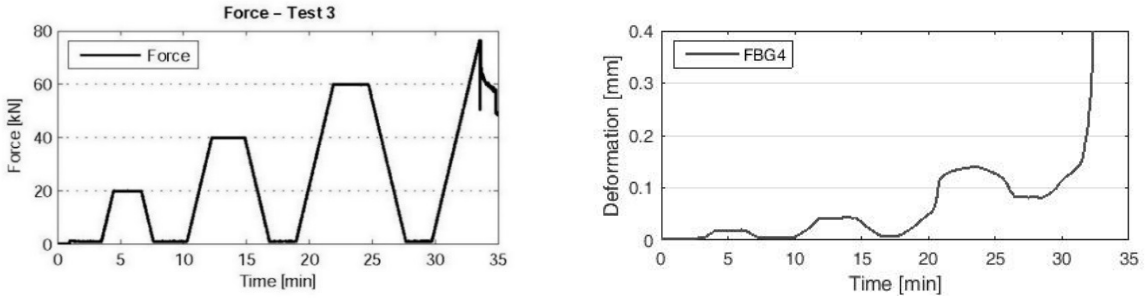

(a) (b)

Figure 2. Applied force (a) and horizontal deformation measured with FBG4 (b) during the cyclic three-point bending test

2.2 Experimental material characterization on small samples

In a dedicated test program, the characteristics of the bricks and mortar were determined. The masonry units were clay bricks with dimensions 188 × 48 × 88 mm^3. The mortar was a hybrid lime-cement mortar composed of river sand 0/2 (68%), Portland cement CEM I 42.5 (5.6 %), hydraulic lime (11.4 %) and water (15%).

The characterization of the flexural strength of both, units and mortar, was done using three-point bending tests on specimens with size 40 × 40 × 160 mm^3 according to EN1015-11 [12]. The tensile strength f_t was indirectly determined as function of flexural strength f_{flex} by means of expression (2), a widely used formula developed for concrete elements, where h_0 means the height of the sample [13]. The testing was performed on three mortar and four unit specimens using a 630 kg_f capacity three-point bending machine.

$$f_t = \frac{0.06\ {h_0}^{0.7}}{1+0.06\ {h_0}^{0.7}} f_{flex} \tag{2}$$

Expression (2) may also be applied to the flexural strength of the masonry member in the direction parallel to the bed joints. The tensile strength obtained thus for the composite is equal to 1.05 N/mm^2.

Compressive strength f_c, Young's modulus E and normal stiffness modulus k_n were derived from uniaxial compression tests on mortar and brick cube samples (Figure 3a). Six mortar samples and eight brick samples with dimensions 40 × 40 × 40 mm^3 were tested. The mortar samples were produced from the two halves of the mortar prisms resulting from the bending test, as per the instructions of the testing standard. The unit samples were produced through cutting with a circular saw, the process itself being sufficient for obtaining accurate dimensions and smooth loading surfaces. No further treatment or compensating layer was applied. The load was applied in displacement control at a rate of 0.2 mm/min in order to accurately register the softening branch. Measurements were taken from four LVDTs which were fixed on the loading plates at each corner of the cubes. Additionally, five polyurethane specimens were also tested to calculate E and k_n for the polyurethane that had been applied as a support layer for the wall. The normal stiffness modulus of the tested materials in the elastic range is calculated by the expression:

$$k_n = \frac{\Delta F}{A \cdot \Delta H} \tag{3}$$

where ΔF is the change in applied load, A is the area of the load surface and ΔH is the change in sample height.A preliminary numerical meso-model, built using the results of these tests, was presented in [11]. In that model, the compressive strength of the joint interfaces $f_{c,i}$ was assumed as the compressive strength of standard masonry $f_{c,m}$ as a function of the brick $f_{c,b}$ and mortar $f_{c,mo}$, following expression (4) from Eurocode 6 [14].

$$f_{c,m} = 0.5\, {f_{c,b}}^{0.7}\, {f_{c,mo}}^{0.3} \tag{4}$$

The normal stiffness of the joint interfaces was estimated from the Young's modulus of the brick E_b and mortar E_{mo}, and thickness of mortar layer $t_{mo,}$ as follows [6]:

$$k_{n,i} = \frac{E_b\, E_{mo}}{t_{mo}\,(E_b - E_{mo})} \tag{5}$$

Expressions (4) and (5) are widely used to characterize the behaviour of masonry and joint interfaces; however, their accuracy depends on the type of mortar and bricks. For instance, expression (5) offers accurate results only if the Young's modulus of the brick is sufficiently higher than that of the mortar, otherwise it results in an unrealistically high normal stiffness.

Therefore, experimental tests on four masonry couplets which were arranged with two bricks bound with a 12 mm mortar layer were also performed. The couplets were tested in compression after 28 days. The load was applied in displacement control at a rate of 0.5 mm/min. Two LVDTs were fixed on the opposite long sides of the couplets, as shown in Figure 3b.

The results of the tests are summarized in Table 1. Strength values showed very little scatter, in contrast to the stiffness properties. The normal stiffness k_n obtained for the couplets (15.3 N/mm^3) is a value in between the stiffness obtained from brick and mortar, and it is much lower than the value calculated using expression (5), which is 17.7x10^3 N/mm^3. The compressive strength f_c of the couplets (5.98 N/mm^2) is also in between the values of its components and is 1.6 times higher than the value calculated using expression (4), which is 3.71 N/mm^2.

It should be noted that the mechanical properties of mortar layers between bricks might vary from the properties of mortar test samples, due to their difference in composition (water from the mortar being absorbed by the bricks during bricklaying), method of compaction and effects of brick-mortar interactions inducing tri-axial stress states. Additionally, the properties of the interfaces in the bed joints may be in practice significantly different from those in the head joints due to lower quality compaction of the mortar in the latter, resulting in reduced adhesion and tensile strength. Identical values were assigned to all interfaces in the numerical modelling carried out in this paper.

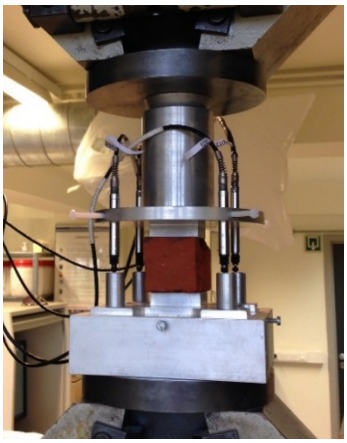

(a)

(b)

Figure 3. Experimental setup for compression tests on cubes (a) and couplets (b)

Table 1. Test results, average of mechanical properties

Material	f_{flex} [N/mm^2]	f_t [N/mm^2]	f_c [N/mm^2]	E [N/mm^2]	k_n [N/mm^3]
Brick	3.65 (0.30)	1.64 (0.14)	9.97 (2.49)	9030 (4771)	17.0 (7.2)
Mortar	1.14 (0.07)	0.50 (0.03)	3.75 (0.42)	8661 (3193)	14.5 (5.4)
Couplets	--	--	5.98 (0.13)	6236 (2236)	15.3 (5.7)
Polyurethane	--	--	--	37.83 (26.68)	0.094* (0.067)

*Equivalent to 150 N/mm.
The standard deviation is indicated in brackets.

The Young's modulus of the couplets measured in the experiments is lower than what would be numerically produced from a uniaxial homogenization of the masonry composite in the direction perpendicular to the bed joint, which would result in a value between the modulus of the brick and that of the mortar in the present case. The homogenization formula reads [7]:

$$E_{masonry} = \frac{t_b + t_{mo}}{\frac{t_b}{E_b} + \frac{t_{mo}}{E_{mo}}} \tag{6}$$

For the present couplet and the calculated Young's moduli of the brick and mortar, expression (6) gives 8927 N/mm^2 for the Young's modulus of the couplet. The discrepancy can be attributed to the imperfect compaction of the mortar in the bed joint, which can result in higher porosity and imperfect adhesion of the mortar to the unit.

3. NUMERICAL MODELS

As mortar joints behave as planes of weakness, masonry has different directional properties. Depending on the required balance between accuracy and simplicity, several strategies have been proposed to model masonry structures. As shown in Figure 4, both a discrete cracking meso-modelling and continuum macro-modelling approaches were implemented in this work to reproduce the experimentally tested wall.

The aim was to simulate the response of the wall under static vertical loading in terms of small deformations, cracking and failure mechanisms, and to determine the influence of material property variations. In addition, the relation between macro-model and meso-model material properties was also addressed. Figure 4 presents the finite element model indicating both strategies used. The model was subjected to a cyclic vertical displacement uniformly applied on a steel plate at the top of the wall, from which the resulting force cycles were obtained.

During the experiment, the area between the concrete block supports was filled with several polyurethane plates. To consider the elastic reaction of this material in the model, springs with different stiffnesses were placed in the nodes at the bottom of the wall. These spring stiffness values were varied based on the arrangement of the plates and results of lab tests performed on the polyurethane samples (values are shown in Table 2).

For all numerical analyses, including the sensitivity study and the calibration of the parameters, a regular Newton Raphson method was employed with a 1% energy, displacement and force norm. The mostly unrestrained situation of the models reduces the build-up of internal forces and the carrying out of the analyses in displacement control reduces the usefulness of the displacement convergence criterion. Nevertheless, the force norm, followed by the energy norm, was the critical convergence criterion for all the steps in the numerical analyses. A line search algorithm was employed to increase the convergence rate.

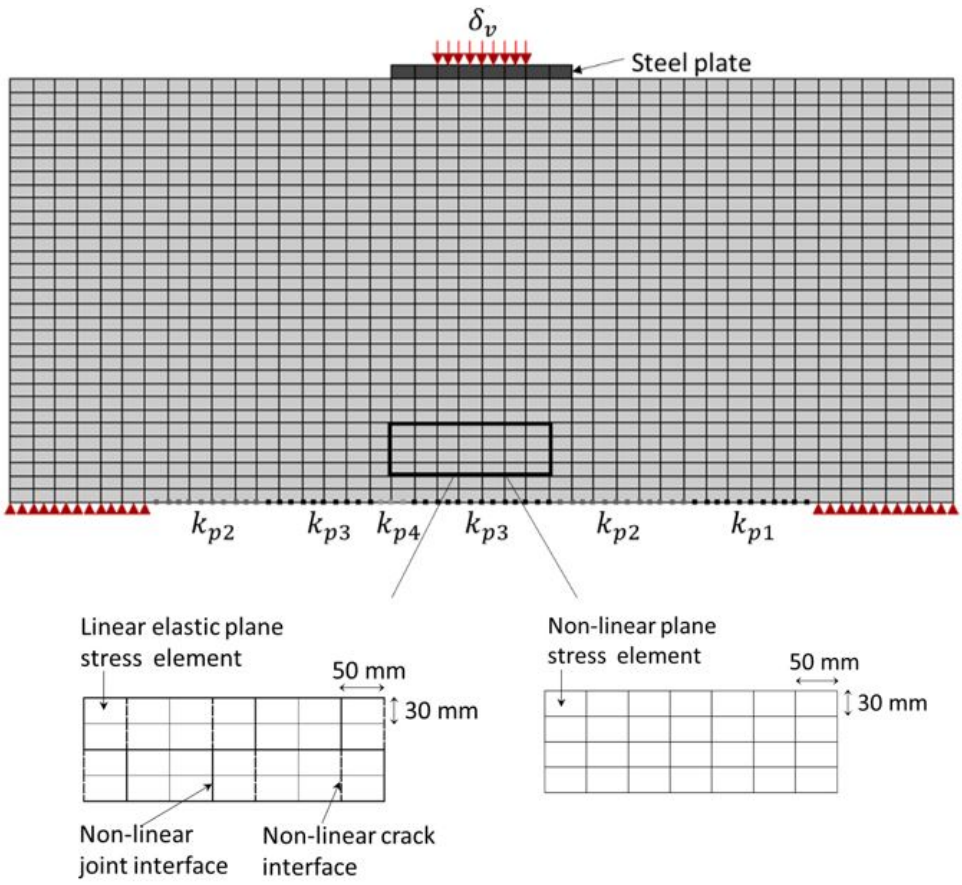

Figure 4. Model of masonry wall showing FE modelling strategies used: Discrete meso-modelling (left), Continuum macro-modelling (right)

Table 2. Material properties for steel plates and polyurethane

Material	Parameter	Sym.	Value	Units
Steel plate	Poisson's ratio	ν_s	0.3	
	Young's modulus	E_s	200000	$\mathrm{N/mm^2}$
Polyurethane	Spring stiffness	k_{p1}	<u>150</u>	$\mathrm{N/mm}$
		k_{p2}	100	
		k_{p3}	50	
		k_{p4}	10	

Note: Underlined value corresponds to lab test result

3.1 Discrete cracking model (meso-modelling)

In the discrete cracking model, the damage was concentrated in relatively weak interfaces simulating the mortar joints by means of discrete non-linear joint interface elements with zero thickness, as shown in Figure 4. The brick elements were expanded to cover half of the width

of the mortar joints and were represented by continuum linear elastic plane stress elements. In addition, non-linear interface elements were used as well to model potential cracks within the bricks (represented with dashed lines in Figure 4).

In this way, masonry was modelled as a set of elastic elements bounded by potential fracture interfaces through the mortar joints and through the bricks. The meso-modelling strategy reduces geometry complexity and computational costs compared to micro-modelling, in which bricks, mortar as well as brick-mortar interfaces are modelled as different elements. However, the main drawback of this approach is the necessity for an approximation of the joint interface non-linear behaviour, for instance, by not accounting for neither the actual stress state in the mortar nor the tri-axial effect generated by the brick/mortar interaction [15].

3.1.1 Pre-processing

The non-linear behaviour of the joint interfaces was modelled using a combined cracking-shearing-crushing model proposed by Lourenço [6, 16]. The plasticity criterion includes three failure mechanisms: joint tensile cracking (Mode I), joint slipping (Mode II) and crushing (Mode III), in which softening behaviour takes place. It is based on multi-surface plasticity and it includes a Coulomb friction model combined with a tension cut-off and an elliptical compression cap [17].

Brick units are represented by quadrilateral continuum plane stress elements, with 8 nodes and 2x2 integration points, arranged as shown in Figure 4. Interface elements with 6 nodes are adopted for both the joints and for the potential cracks.

3.1.2 Selection of material properties

In the conventional approach, material properties are directly derived from experimental tests on small samples of both brick and mortar. However, this approach might not be representative of the masonry arrangement whose behaviour is intrinsically inhomogeneous. In addition, brick and mortar samples have highly variable properties depending on their composition and manufacturing processes.

Some authors have proposed methods for material parameter identification of discrete cracking models based on optimization of the responses of large scale masonry elements (e.g. [18]). However, these methods are good strategies as long as large scale experimental tests are available, which is not the current case.

The approach adopted in this work aimed to determine reference masonry properties by means of a calibration through series of numerical analyses and parameter sensitivity analyses [19, 20], which are based on laboratory tests on small specimens (Table 1) as well as a wide range of data from the literature (Table 3).

The compressive strength of the joints $f_{c,i}$ was assumed as the value obtained from the tested masonry couplets. The compressive fracture energy $G_{c,i}$ was calculated assuming a ductility index parameter of 1 mm, defined as [15]:

$$d = G_{c,i}/f_{c,i} \tag{7}$$

Note that a high elastic dummy stiffness is considered for the potential cracks in the bricks. The tensile strength for the potential crack interface $f_{t,b}$ was assumed equal to the tensile strength of the tested brick samples. Literature values for the ratio between joint normal and shear stiffness $k_{n,i}/k_{s,i}$ range from 2.18 to 2.5 [21]; for the current study, this ratio was assumed equal to 2.4.

The internal friction angle ϕ_i was assumed equal to the residual friction angle ϕ_r. The dilatancy angle ψ was taken equal to zero, due to the sample being unconfined, thus, rendering the dilatancy of the interface elements of low relevance [6]. The plastic relative displacement k_p, which controls the softening behaviour, is considered equal to 0.093 [6]. The parameter C_{ss} which controls the contribution of the shear stress to compressive failure is considered equal to 9.0 [6].

Regarding values of cohesion of joints c_i, Lourenço [6] recommend values near 1.4 $f_{t,i}$, when there is lack of data. Moreover, according to experimental results presented by Van der Pluijm [22], c_i can vary from 0.3 $f_{t,i}$ to 2.0 $f_{t,i}$.

Table 3. Properties of masonry components from literature

Material	Parameter	Sym.	Value [Ref.]	Units
Brick unit	Young's modulus	E_b	976[15], 3372[15], 4865[15], 6050[18], 7750[6], 8000 [20], 12000[15], 16700[23]	$\mathrm{N/mm^2}$
Joints	Normal stiffness	$k_{n,i}$	13.5[18], 82[7], 180[6], 550[20]	$\mathrm{N/mm^3}$
	Shear stiffness	$k_{s,i}$	5.9[18], 36[7], 80[6], 210[20]	$\mathrm{N/mm^3}$
	Tensile strength	$f_{t,i}$	0.1[18, 20], 0.2[15], 0.25[7], 0.29[6], (0.3-0.9)[22] , 7.6[24]	$\mathrm{N/mm^2}$
	Tensile fracture energy (Mode I)	$G_{t,i}$	0.01[7, 20, 24] , 0.0115[23], 0.012[15], 0.02[6], (0.005 - 0.02)[22]	$\mathrm{N/mm}$
	Cohesion	c_i	0.25[15], 0.375[7], 0.41[6], (0.1-1.8)[22]	$\mathrm{N/mm^2}$
	Friction angle	Φ_i	36.9 [6, 7], 45[15]	°
	Shear fracture energy (Mode II)	$G_{s,i}$	0.025[15], 0.05[6], 0.125[6], (0.01-0.25)[22]	$\mathrm{N/mm}$

Note: [24] refers to cement based mortar joints

3.1.3 Discrete model calibration

In a next step, material properties for the discrete cracking model such as E_b, $k_{n,i}$, $f_{t,i}$, $G_{t,I}$ and c_i were calibrated. Therefore, series of computational experiments were carried out, in which these material properties were initially assigned based on the laboratory test results on small specimens (Table 1) and a wide range of data from literature (Table 3). The effect of each parameter variation was evaluated independently from the others, except for shear stiffness and cohesion which were related to normal stiffness and tensile strength, respectively. The rest of model parameters were not altered in this calibration process.

The most representative material parameters used in the calibration are shown in Table 4. The values that fitted the best the experimental results were adopted as reference. The model performance was evaluated against the ultimate load vs the related vertical displacement and the horizontal deformations leading to cracking.

For instance, Figures 5a–9a show the numerical force-vertical displacement curves for each material property variation, indicating the peak load and experimental values. Figures 5b–9b present the horizontal deformation in terms of relative displacement between nodes A and B at the anchorage points of FBG4 (see Figure 1). Reference values that were determined based on this calibration are indicated with *.

Table 4. Representative values used in the discrete cracking model calibration

Material	Parameter	Sym.	Value	Units
Brick unit	Density	ρ_b	1875	$\mathrm{kg/m^3}$
	Poisson's ratio	ν_b	0.15	
	Young's modulus	$\boldsymbol{E_b}$	**976, (2000), 6236, 9030**	$\mathrm{N/mm^2}$
Crack interfaces in brick units	Normal stiffness	$k_{n,b}$	10000	$\mathrm{N/mm^3}$
	Shear stiffness	$k_{s,b}$	1000	$\mathrm{N/mm^3}$
	Tensile strength	$f_{t,b}$	1.64	$\mathrm{N/mm^2}$
	Cohesion	c_b	$1.4\ f_{t,b}$	$\mathrm{N/mm^2}$
	Friction angle	Φ_b	45	°
Joint interfaces	**Normal stiffness**	$\boldsymbol{k_{n,i}}$	**(15.3), 82, 180, 550**	$\mathrm{N/mm^3}$
	Shear stiffness	$k_{s,i}$	$k_{n,i}/2.4$	$\mathrm{N/mm^3}$
	Tensile strength	$\boldsymbol{f_{t,i}}$	**(0.15), 0.25, 0.5, 0.9**	$\mathrm{N/mm^2}$
	Tensile fracture energy	$\boldsymbol{G_{t,i}}$	**0.012, 0.02, 0.07, (0.115)**	$\mathrm{N/mm}$
	Cohesion	$\boldsymbol{c_i}$	$\boldsymbol{1.0\ f_{t,i}}$, $\boldsymbol{1.4\ f_{t,i}}$, $(\boldsymbol{1.86 f_{t,i}})$, $\boldsymbol{2.0 f_{t,i}}$	$\mathrm{N/mm^2}$
	Friction angle	Φ_i	36.9	°
	Dilatancy angle	ψ_i	0	°

Shear fracture energy (Mode II)	$G_{s,i}$	0.125	$\mathrm{N/mm}$
Compressive strength	$f_{c,i}$	<u>5.98</u>	$\mathrm{N/mm^2}$
Compressive fracture energy	$G_{c,i}$	5.98	$\mathrm{N/mm}$

Note: Values in bold are the parameters used in the calibration. Values in parentheses are the adopted reference values. Underlined values correspond to laboratory testing on small samples (section 2.2).

It was observed that both the normal stiffness of the joint interfaces k_n, and the Young's modulus of the brick unit E_b, significantly affect the global stiffness of the wall (Figure 5a and Figure 6a). However, E_b has much higher influence on the deformations (Figure 5b and Figure 6b).

A reduction in tensile fracture energy of joint interfaces $G_{t,i}$, leads to a lower load capacity, without significantly affecting the horizontal deformation, as shown in Figure 7.

Figure 8 indicates that the higher the tensile strength $f_{t,i}$, the more brittle the failure is; the $f_{t,I}$ variation moderately affecting the crack width. Furthermore, the cohesion of the joint interfaces c_i has limited influence on the load capacity, but considerably influences the horizontal deformations after cracking, as can be seen from Figure 9.

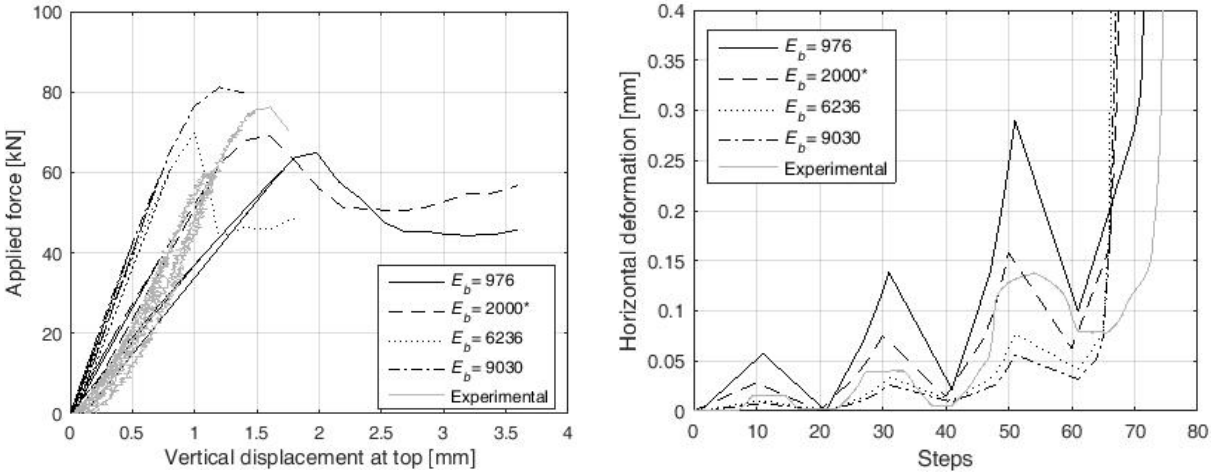

Figure 5. Discrete model calibration: (a) force-vertical displacement graphs and (b) load step-horizontal displacement graphs for variation of Young's modulus of brick unit

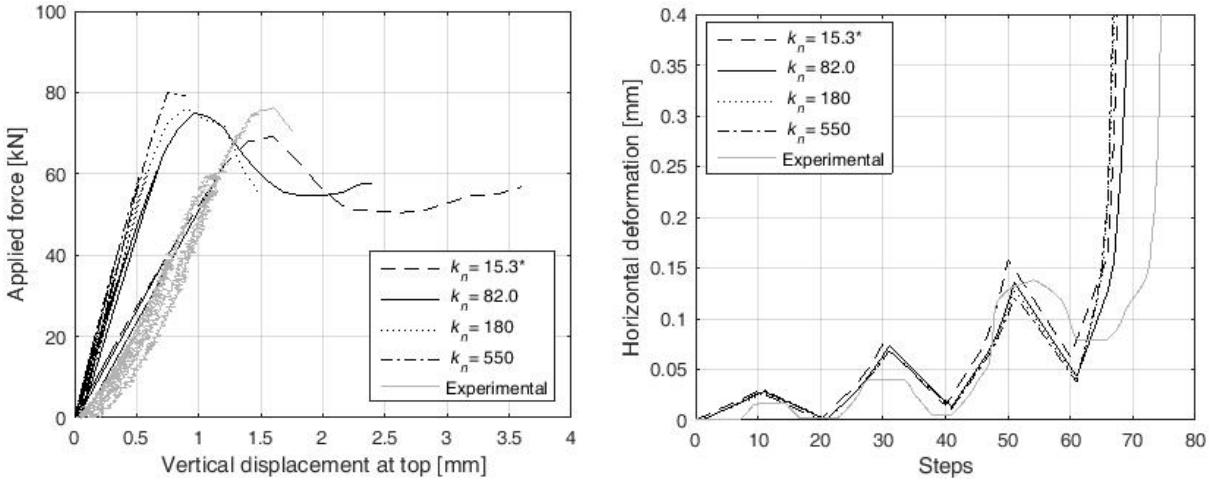

(a) (b)

Figure 6. Discrete model calibration: (a) force-vertical displacement graphs and (b) load step-horizontal displacement graphs for variation of normal stiffness of joint interfaces

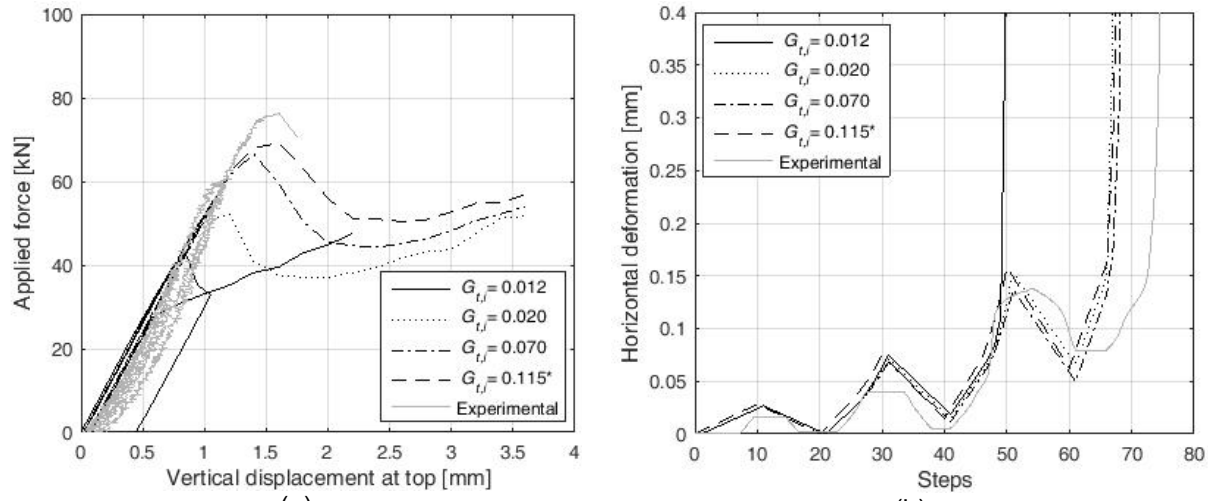

(a) (b)

Figure 7. Discrete model calibration: (a) force-vertical displacement graphs and (b) load step-horizontal displacement graphs for variation of tensile fracture energy of joint interfaces

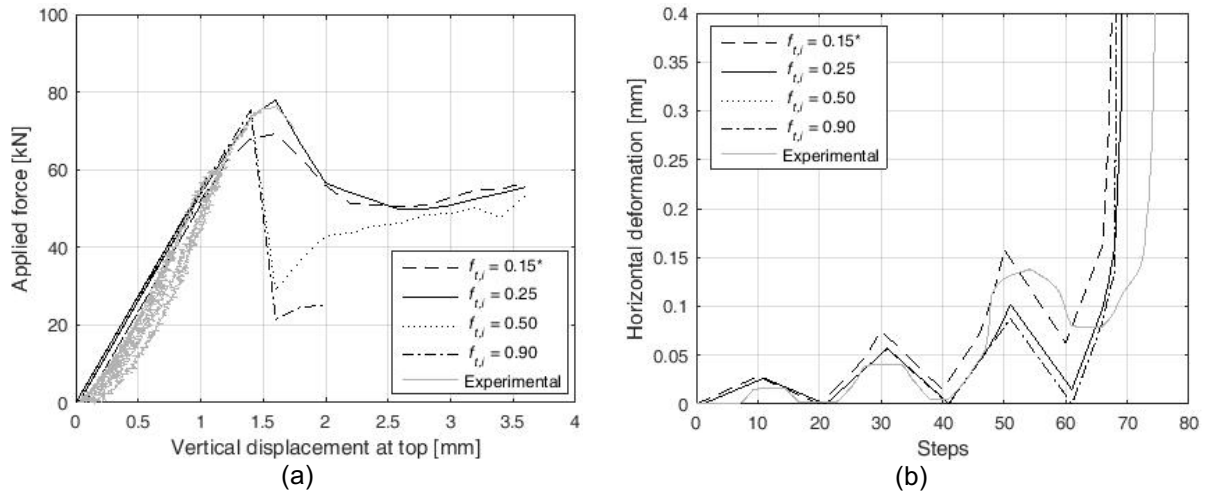

(a) (b)

Figure 8. Discrete model calibration: (a) force-vertical displacement graphs and (b) load step-horizontal displacement graphs for variation of tensile strength of joint interfaces

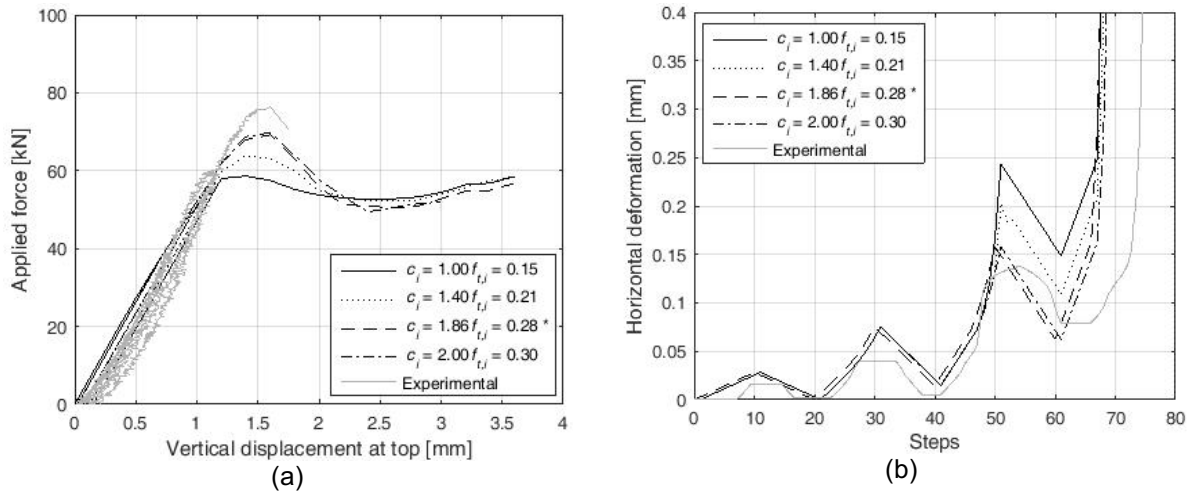

(a) (b)

Figure 9. Discrete model calibration: (a) force-vertical displacement graphs and (b) load step-horizontal displacement graphs for variation of cohesion of joint interfaces

3.2 Continuum smeared cracking model (macro-modelling)

Within the macro-modelling strategy, bricks, mortar and brick-mortar interfaces are smeared out in a homogeneous anisotropic continuum composite without considering their interaction (Figure 4). Therefore, a general relation between average stresses and strains in the composite material is considered. This strategy is mainly practice oriented to reduce calculation costs and allow a user-friendly mesh generation [6].

3.2.1 Pre-processing

In the continuum smeared cracking approach, a multi–directional fixed crack model was adopted, in which cracking is specified as a combination of linear tension cut-off, tension softening and shear retention [17]. A full shear retention was assumed which implies that the elastic shear modulus is not reduced. The tension softening law is defined by the tensile strength of the composite masonry $f_{t,m}$, the tensile fracture energy $G_{t,m}$, and the crack bandwidth h, which is related to the size of the element (30x50 mm²) and assumed equal to 40 mm. The ultimate crack strain is calculated as:

$$\varepsilon_m^{cr} = \frac{2G_{t,m}}{f_{t,m}\ h} \tag{8}$$

The wall was modelled using 8-node quadrilateral plane stress elements with 2x2 Gaussian integration points, as for the discrete cracking model.

3.2.2 Selection of material properties

Limited experimental test data for the mechanical properties of composite masonry are available in literature, especially for those properties that determine the cracking behaviour such as tensile strength $f_{t,m}$ and fracture energy $G_{t,m}$. Moreover, cracking behaviour is

influenced by other factors such as loading, type of components and bond type. Therefore, as an attempt to determine the properties of composite masonry as a function of the properties of its components, the methodology proposed by Noort [25] was implemented.

This methodology uses extra numerical analyses to obtain the material properties of the continuum smeared model from a discrete cracking model. For that purpose, discrete cracking models of small masonry panels are subjected to tension and compression to numerically determine the stress-strain curves and fracture energies of the composite.

For this work, masonry panels with size 500x360x188 mm were simulated and subjected to tension and compression as indicated in Figure 10. The material properties and element types used for these discrete cracking models are the final reference values adopted for the wall model presented in Section 3.1, considering both joint and crack interfaces. The analyses were performed applying a controlled increasing displacement to the very rigid boundary plates.

The simulated stress-strain curves for all panel models are presented in Figure 11. These curves clearly show the orthotropic behaviour of the discrete masonry model by exhibiting higher stiffness in the horizontal direction when load is applied parallel to the bed joints. Ultimate tensile strength parallel to bed joints is also higher; this effect might be influenced by the higher tensile strength of the crack interfaces in the brick units and the shear stress arising in the interface between the unit and the bed joint mortar.

Failure in compression in both loading directions was due to compressive failure of the interfaces perpendicular to the direction of the load, with minimal influence of the opening of the interfaces parallel to the direction of the load. The latter generally includes the unit-mortar interfaces and, in the case of loading perpendicular to the bed joints, the potential cracks in the units. For tensile loading perpendicular to the bed joints the failure was due to the opening of the bed joints. Under tensile loading parallel to the bed joints a stepped crack was obtained caused by the staggered arrangement of the head joints. The potential cracks in the units failed to open, with the tensile strength of the composite in this direction being supplied by the tensile strength of head joints and the shear contribution of the bed joints.

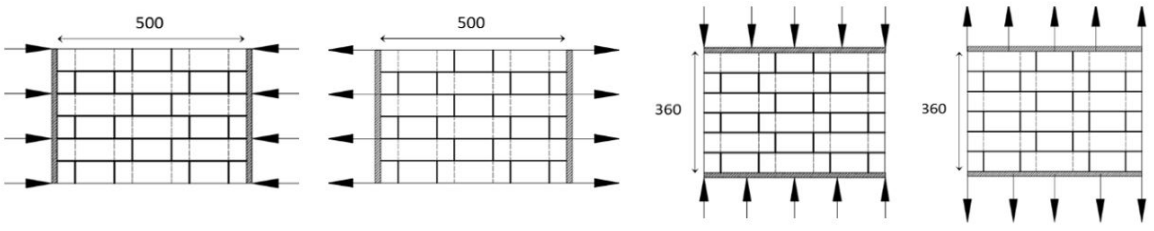

Figure 10. Discrete cracking models of masonry panels under compression and tension. (a) Load applied parallel to bed joints. (b) Load applied perpendicular to bed joints (dimensions are in mm)

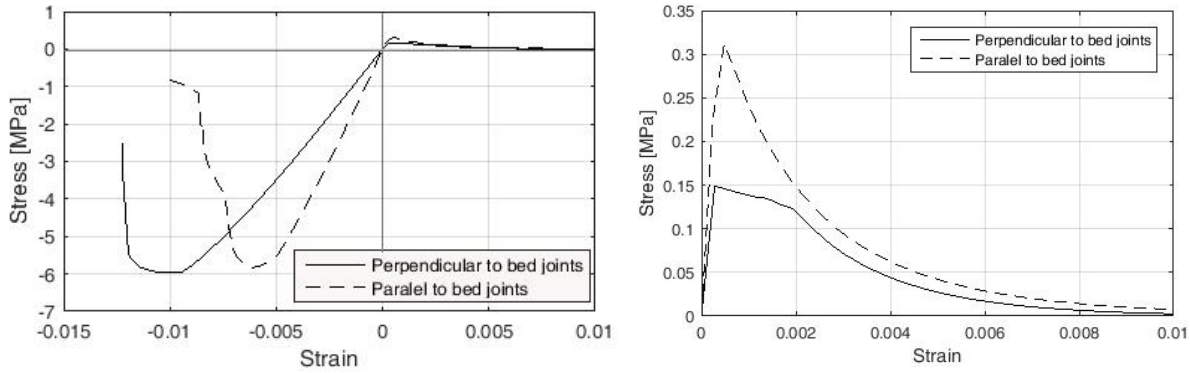

Figure 11. Stress-strain curves of panel models. (a) compression (negative values) and tension behaviour (positive values). (b) zoom in on tension behaviour

Young's modulus E_m, tensile strength $f_{t,m}$ and tensile fracture energy $G_{t,m}$ for the composite masonry were determined from the stress-strain curves of the panel models for loading applied parallel and as perpendicular to bed joints. $G_{t,m}$ was obtained by multiplying the area under the post-peak part of the curve by the corresponding panel side effective length.

3.2.3 Continuum model calibration

Similarly to the discrete cracking model, a calibration procedure was carried out in order to identify reference values and analyse the influence of material properties on the mechanical response of the wall. The material properties used for this calibration were E_m, $f_{t,m}$ and $G_{t,m}$. A series of computational experiments were performed in which these properties were defined according to the numerical results obtained from the masonry panels, laboratory test results on small specimens (Table 1) and experimental results from literature (Table 5).

The most representative material properties from the calibration are shown in Table 6. This table also indicates the adopted reference values which best fitted the experimental results in terms of ultimate load vs vertical displacement and horizontal deformations leading to cracking. The values with superscripts *pe* and *pa* correspond to the results obtained from the panel models for loading perpendicular and parallel to the bed joints, respectively.

Table 5. Composite masonry properties from literature

Parameter	Sym.	Value [Ref.]	Units
Young's modulus	E_m	1211[26], 1410[23],1651[15], 1868[26], 2090[27], 2800[27], 3000[20], 3833[15], 4567[15], 5000[6], 5600[28], 28000[24]	$\mathrm{N/mm^2}$
Tensile strength	$f_{t,m}$	0.1[20], 0.3[23], 0.5[6], 5.8[24]	$\mathrm{N/mm^2}$
Fracture energy	$G_{t,m}$	0.01[6, 20], 0.0115[23], 0.075[24]	$\mathrm{N/mm}$

Table 6. Representative values used in the continuum model

Parameter	Symb.	Value	Units
Density	ρ_m	1875	kg/m^3
Poisson's ratio	ν_m	0.15	
Young's modulus	$\boldsymbol{E_m}$	**661^{pe}, (1126^{pa}), 3000, 6236**	N/mm^2
Tensile strength	$\boldsymbol{f_{t,m}}$	**0.15^{pe}, (0.31^{pa}), 0.4, 0.5**	N/mm^2
Compressive strength	$f_{c,m}$	5.98	N/mm^2
Fracture energy	$\boldsymbol{G_{t,m}}$	**0.01, 0.075, 0.17^{pe}, (0.32^{pa})**	N/mm

Note: Values in bold are the parameters used in the calibration. Values in parentheses are the adopted reference values. Underlined values correspond to laboratory testing on small samples (section 2.2).

Figures 12a-14a show the force-vertical displacement curves for the representative values, in which adopted reference values are indicated with *. It was found that *pa* values, corresponding to the panel loaded parallel to the bed joints, fitted the experimental results best.

The curves show a marked brittle failure characterized by a rapid decrease of strength after peak loading. Furthermore, the mechanical behaviour of the wall was dominated by the three analysed properties.

Figure 12 indicates that the Young's modulus E_m significantly affects both the global stiffness of the wall and the deformations, similar to the meso-model. In this work, the Young's modulus obtained from compression tests on small samples, in this case couplets (6236 MPa), resulted to be very high to characterize the composed masonry in three-point bending, a fact that should be taken into account for further model calibrations.

The tensile strength of composed masonry $f_{t,m}$ exhibits a much higher influence on both load capacity and deformations (Figure 13), in comparison with the tensile strength of joint interfaces $f_{t,i}$ used for the meso-model. Figure 13.b shows that for $f_{t,m}$ = 0.15 MPa, the deformations are much larger than experimental data.

A lower fracture energy $G_{t,m}$ induces a lower load capacity, slightly affecting horizontal deformations, as illustrated in Figure 14. For $G_{t,m}$=0.01 N/mm, the failure already occurred in the third load cycle for an applied force of 46 kN.

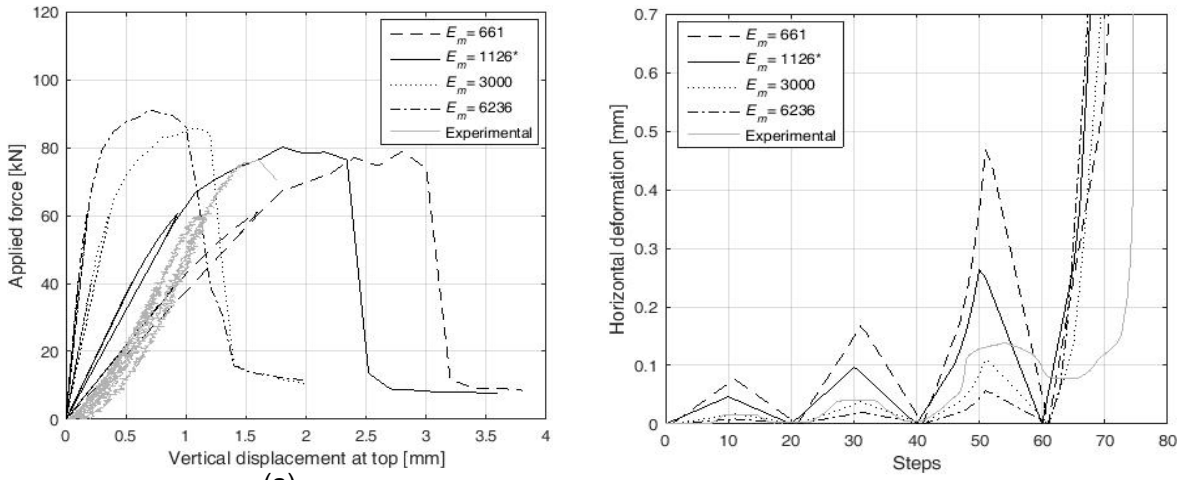

(a) (b)

Figure 12. Continuum model calibration: (a) force-vertical displacement graphs and (b) load step-horizontal displacement graphs for variation of Young's modulus of composed masonry

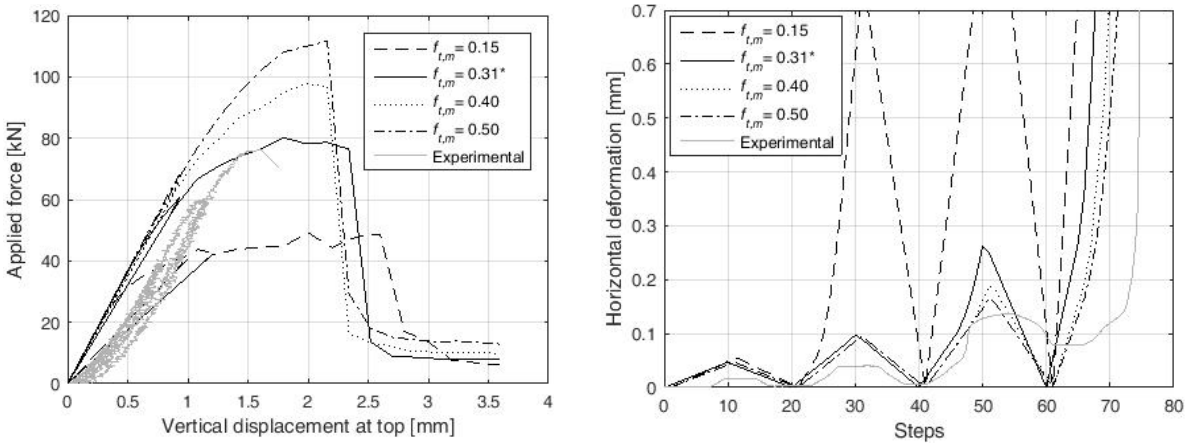

(a) (b)

Figure 13. Continuum model calibration: (a) force-vertical displacement graphs and (b) load step-horizontal displacement graphs for variation of tensile strength of composed masonry

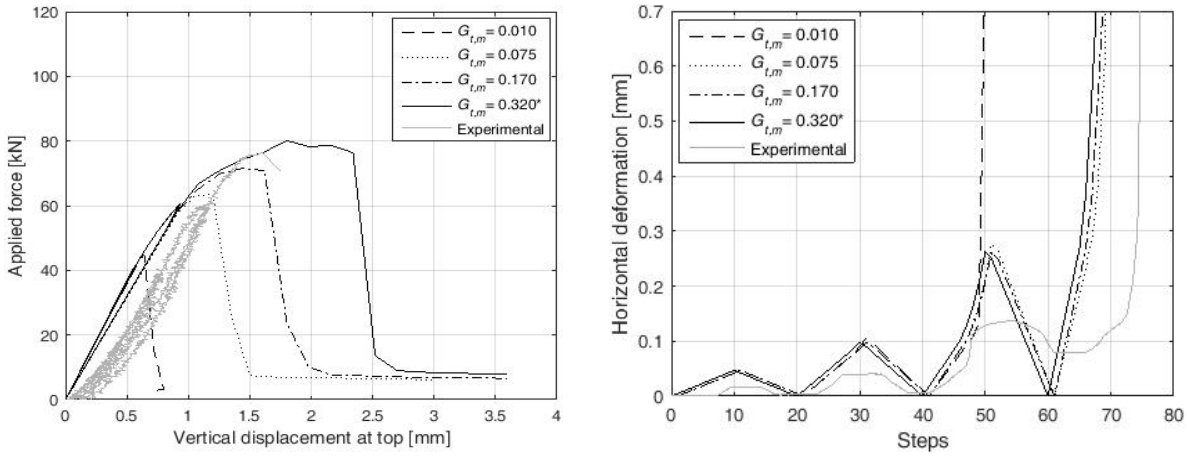

(a) (b)

Figure 14. Continuum model calibration: (a) force-vertical displacement graphs and (b) load step-horizontal displacement graphs for variation of tensile fracture energy of composed masonry

4. MODEL VALIDATION

This section presents the results of analyses performed by using both modelling strategies with reference material properties obtained from the calibration procedure. All the numerical analyses were performed in displacement control using the cycling loading scheme employed in the experimental test (Figure 2a). Three load-unload cycles, up to 20, 40 and 60 kN, and a fourth load cycle, up to the peak load, were split into 81 analysis steps. Figure 15a shows the cycle load implemented for both models, together with the experimental loading scheme (steps of experimental data were scaled from time records). The force-displacement curves from experimental data and numerical results match well throughout all the steps, as shown in Figure 15b. Vertical displacement refers to the nodes at the top of the wall, where the load was applied. The collapse load obtained from the experiment was 76.4 kN, which is in between the values obtained by using the meso-model (69.2 kN) and the macro-model (80.1 kN). The continuum macro-model presents a marked softening behaviour, decreasing strength rapidly after the peak, while the discrete meso-model shows some ductility after peak loading. The calculation time with the meso-model is three times longer than the calculation with the macro-model.

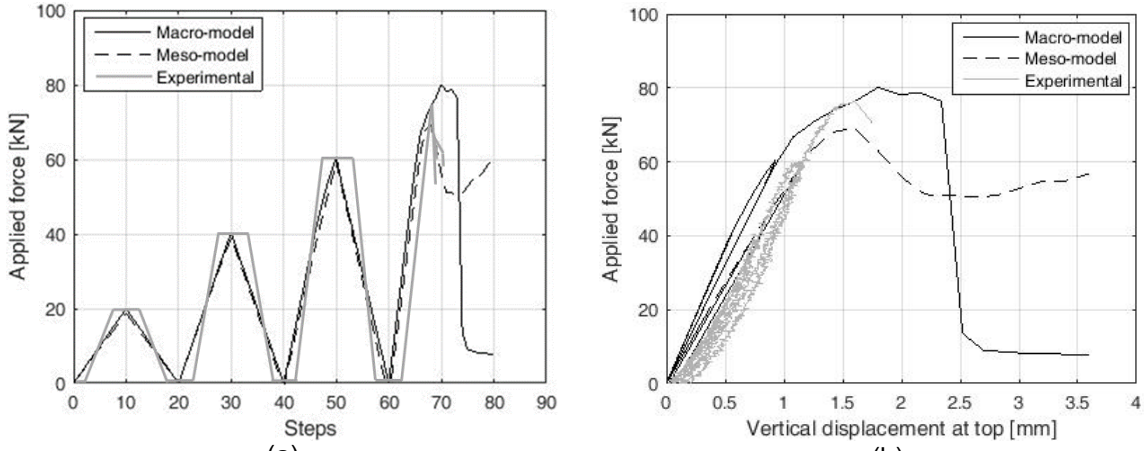

Figure 15. Comparison between experimental and numerical approaches:
(a) cycling load; (b) force-displacement curve

During the experimental test, small vertical cracks were visually observed in the mortar joints and lower bricks in the third load cycle (60 kN). Assuming that all the horizontal deformation is lumped in the crack after its formation, the experimentally obtained crack width in the plateau of the third cycle was 0.14 mm. The meso-model produced a crack width of 0.16 mm and the macro-model a crack width of 0.26 mm. During the next load cycle, these cracks coalesced into a large crack (Figure 16). The test was ended shortly after the appearance of this large crack. This crack did not appear in the middle of the wall, presumably due to asymmetrical boundary conditions corresponding to the distribution of the polyurethane plates. This

phenomenon was considered in the model by arranging different spring stiffnesses as mentioned in Section 3.

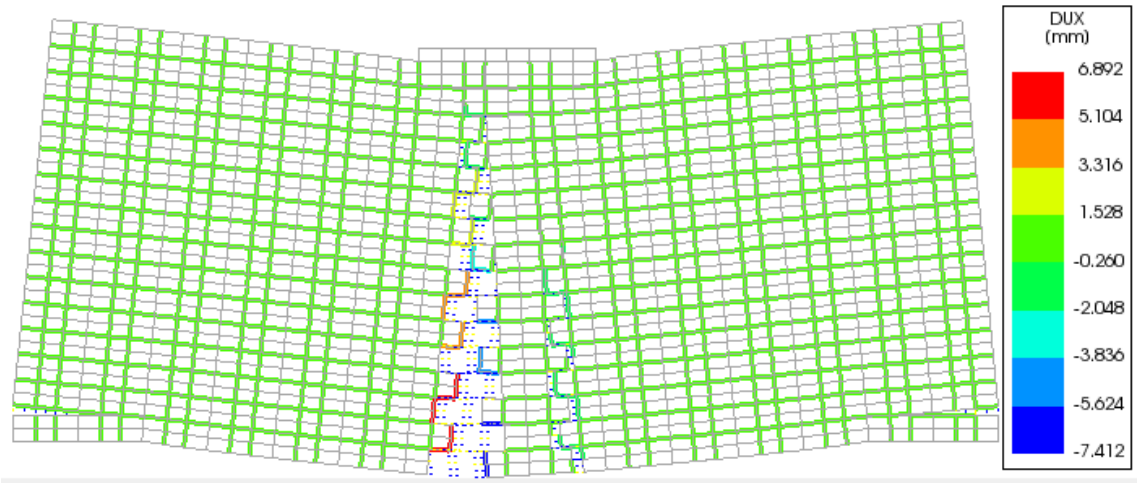

(a)

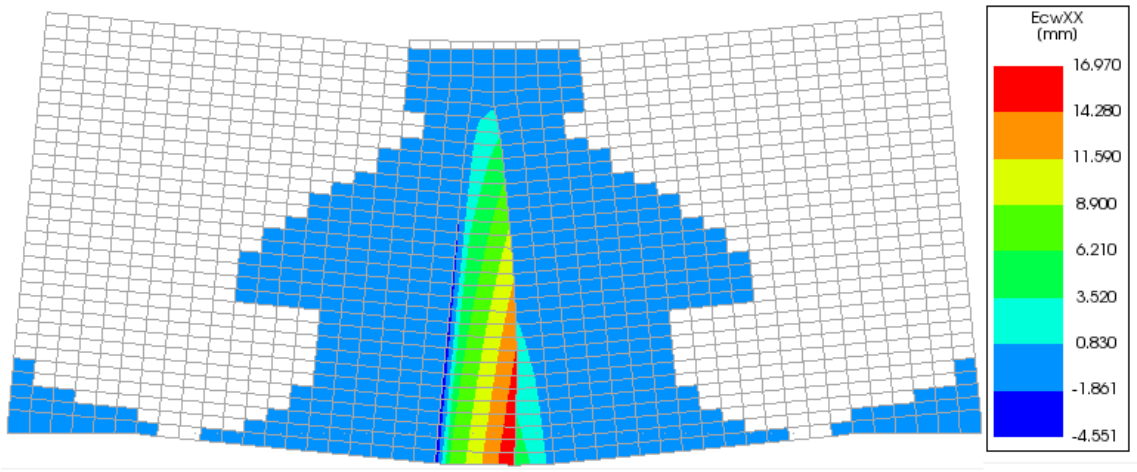

(b)

Figure 17 shows the failure mechanisms of both models. They present similar deformed shape, with the meso-model presenting a more accurate location of the major crack. The macro-model showed a final crack width at the bottom of the wall equal to 16.9 mm, slightly wider than the value obtained with the meso-model (14.3 mm).

Figure 18 shows the evolution of horizontal deformation from experimental data and numerical models, related to the location of sensor FBG4 [11]. The horizontal deformation from the numerical models is based on the relative displacement between the nodes located in the positions A and B at the anchorage points of FBG4 (see Figure 1). Since the fracture is very brittle, large deformations occurred just after the peak load during the fourth load cycle. These

deformations were larger in the macro-model than in the meso-model. In the initial three load cycles (Figure 18b), where elastic deformations and micro cracking were taking place, the results from the macro-model are more conservative, presenting larger horizontal deformations by roughly 73% compared to the meso-model at the plateau of the third cycle and 12% at the end of the loading. However, the horizontal deformation results from the meso-model are closer to the experimental values, and they clearly show the unrecovered deformations monitored during the third unloading cycle.

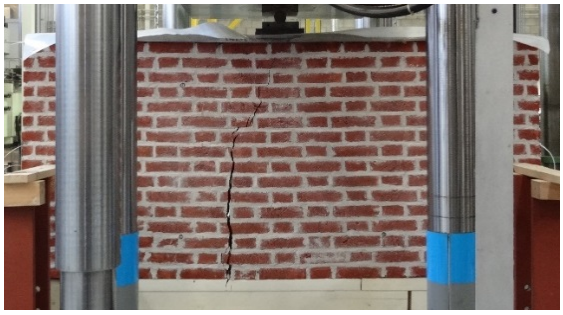

Figure 16. Picture of the wall after testing showing the major crack

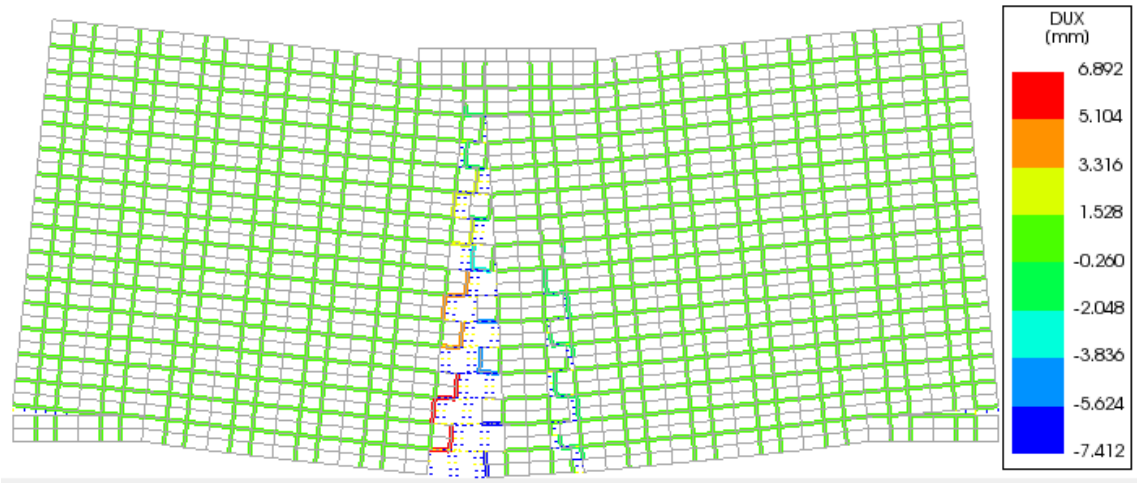

(a)

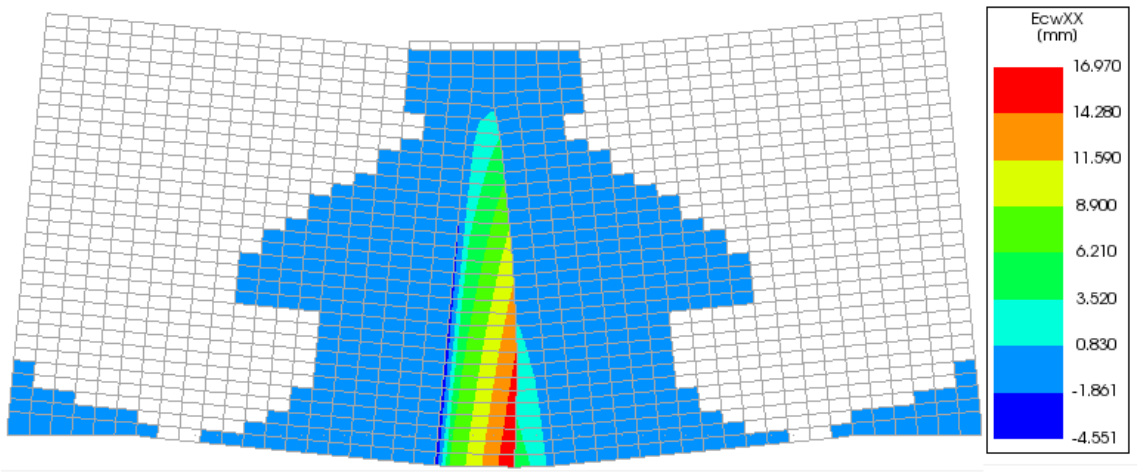

(b)

Figure 17. Final deformed mesh showing: (a) horizontal interface displacements in meso-model, (b) horizontal crack widths in macro-model

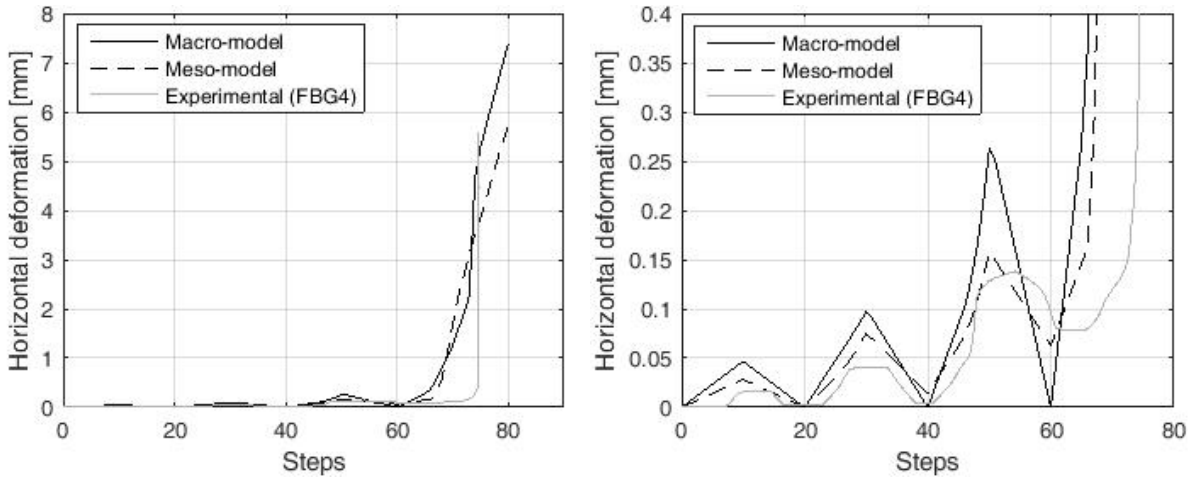

(a) (b)

Figure 18. Comparison between experimentally measured and numerically obtained horizontal deformation. (a) Entire simulation, high deformations. (b) Initial three load cycles, low deformations.

Figure 19a presents the measured vertical displacement field u_y as a function of the surface coordinates at 60 kN of the fourth load cycle, before failure, while Figure 20a shows the measured horizontal displacement field u_x after failure. Measurements were recorded in the area of interest with digital image correlation (DIC) without the use of a speckle pattern[11]. Figure 19b and Figure 20b show the corresponding contour maps related to the displacement field obtained from the meso-model, whereas Figure 19,c and Figure 20,c present the corresponding contour maps of displacement fields obtained from the macro-model. The numerical results of the vertical displacement field show displacements similar to the experimental data. The maximum vertical displacement values are about 1.1 mm for the

numerical models and about 1.0 mm for the test. Figure 20 shows very clearly the location and shape of the major crack. It can be seen that the crack tip acts as a hinge: the lower the position, the higher the horizontal displacement. The left part rotates clockwise around the crack tip, whereas the right part rotates counter clockwise.

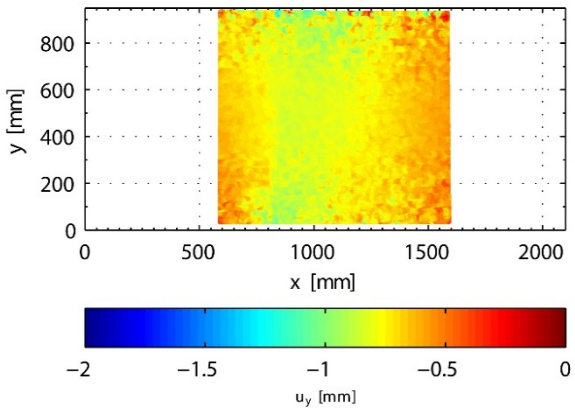

(a)

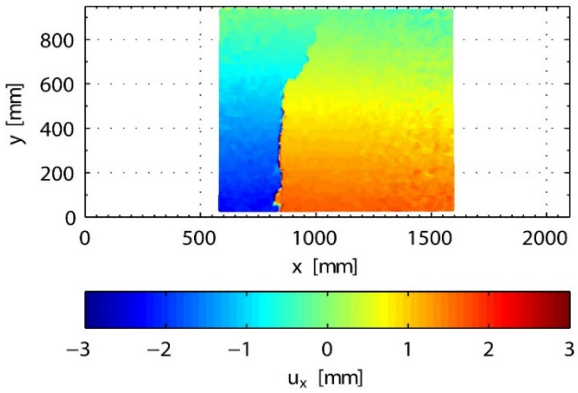

(a)

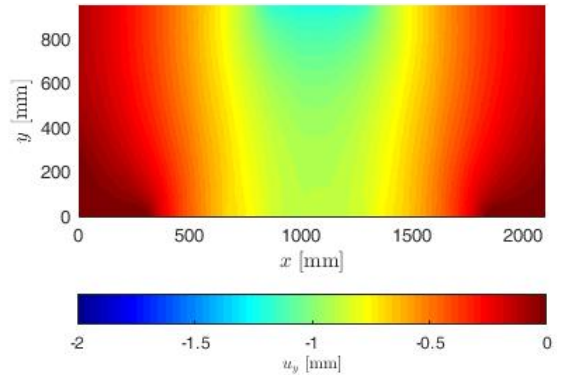

(b)

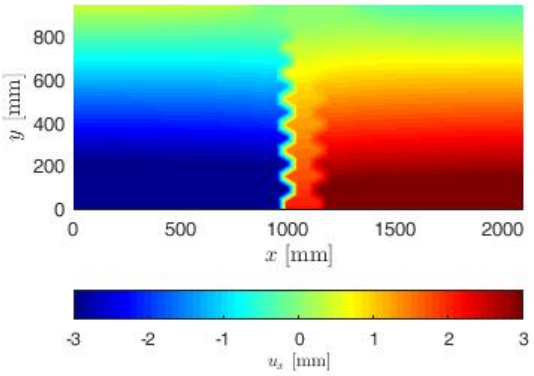

(b)

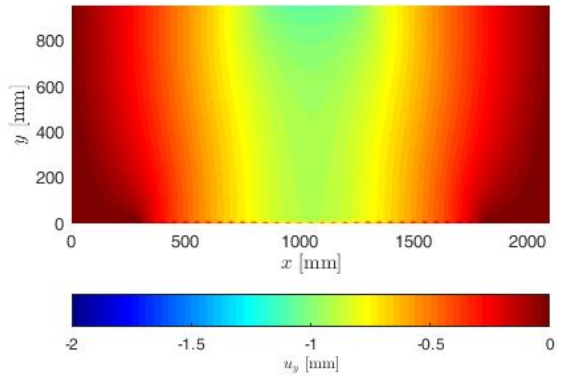

(c)

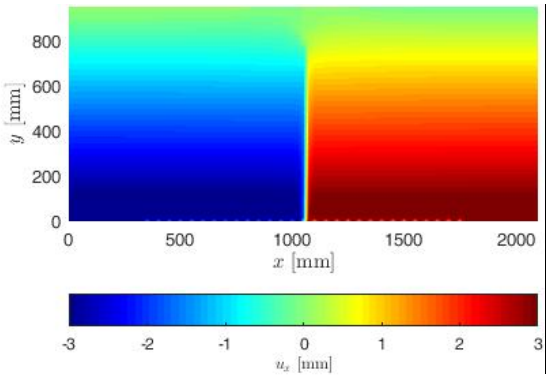

(c)

Figure 19. Vertical displacement field u_y at 60 kN of the fourth load cycle before failure. (a) experimental results from DIC. (b) meso-model. (c) macro-model

Figure 20. Horizontal displacement field u_x after failure. (a) experimental results from DIC. (b) meso-model. (c) macro-model

Both numerical modelling approaches presented results in good agreement with the experimental data in terms of load capacity, horizontal displacements and failure mechanism. The meso-model showed better accuracy, being able to represent unrecoverable deformations. The macro-model is more conservative, showing higher deformation values.

5. SUMMARIZED RESULTS OF SENSITIVITY STUDY

Table 7 and Table 8 indicate the representative material properties obtained from the calibration procedure (Sections 3.1.3 and 3.2.3). Sensitivity studies were performed to investigate the effect of the variation of this set of material properties on the mechanical behaviour of the wall with respect to peak load and horizontal deformation leading to cracking.

Table 7. Range of values used in the sensitivity analysis within the discrete cracking model

Material	Property	Sym.	Reference value, V_R	Units	Value, V	V / V_R
Brick unit	Young's modulus	E_b	2000	$\mathrm{N/mm^2}$	976, 6236, 9030	0.49, 3.12, 4.52
Joint interface	Normal stiffness	$k_{n,i}$	15.3	$\mathrm{N/mm^3}$	82, 180, 550	5.36, 11.76, 35.95
	Tensile strength	$f_{t,i}$	0.15	$\mathrm{N/mm^2}$	0.25, 0.50, 0.90	1.67, 3.33, 6.00
	Tensile fracture energy	$G_{t,i}$	0.115	$\mathrm{N/mm}$	0.012, 0.02, 0.07	0.10, 0.17, 0.61
	Cohesion	c_i	$1.86 f_{t,i}$	$\mathrm{N/mm^2}$	$1.0\ f_{t,i}, 1.4\ f_{t,i}, 2.0 f_{t,i}$	0.54, 0.75, 1.08

Table 8. Range of values used in the sensitivity analysis within the continuum model

Property	Sym.	Ref. value, V_R	Units	Value, V	V/ V_R
Young's modulus	E_m	1126^{pa}	$\mathrm{N/mm^2}$	661^{pe}, 3000, 6236	0.59, 2.66, 5.54
Tensile strength	$f_{t,m}$	0.31^{pa}	$\mathrm{N/mm^2}$	0.15^{pe}, 0.40, 0.50	0.48, 1.29, 1.61
Fracture energy	$G_{t,m}$	0.32^{pa}	$\mathrm{N/mm}$	0.01, 0.075, 0.17^{pe}	0.06, 0.44, 1.88

Figure 21 and Figure 22 show the influence of variation of the different material properties on the peak load and the horizontal deformation at the third loading cycle (60 kN), for the meso- and macro-model, respectively. As before, this horizontal deformation is related to the points A and B (see Figure 1). The corresponding experimental values are indicated with a dotted horizontal line. Normalized values refer to the ratio between the current and reference value for each material property used in the sensitivity analysis.

As shown in Figure 21, the tensile fracture energy of the interfaces $G_{t,i}$ and the cohesion c_i have an important influence on both the load capacity and cracking in the meso-model. These are critical properties, since a small variation in $G_{t,i}$ and c_i can have a significant influence in the peak load and horizontal deformation. The formation of a stepped crack in the discrete crack models causes the cohesion to emerge as a significant parameter affecting the peak force obtained by analysis. The activation of this shearing mechanism, which would otherwise not be activated in pure bending without applied vertical stress, is the possible result of the support provided by the polyurethane plates. Vertical compressive stress arises between the springs and the press, causing the bed joint interfaces to more markedly contribute through shear to the transfer of horizontal forces. The normal stiffness $k_{n,i}$ and the tensile strength $f_{t,i}$ show a smaller influence on the results.

For the macro-model, Young's modulus, fracture energy and tensile strength all have a considerable influence on load capacity and deformation, being $G_{t,m}$ and $f_{t,m}$ the dominant factors (Figure 22).

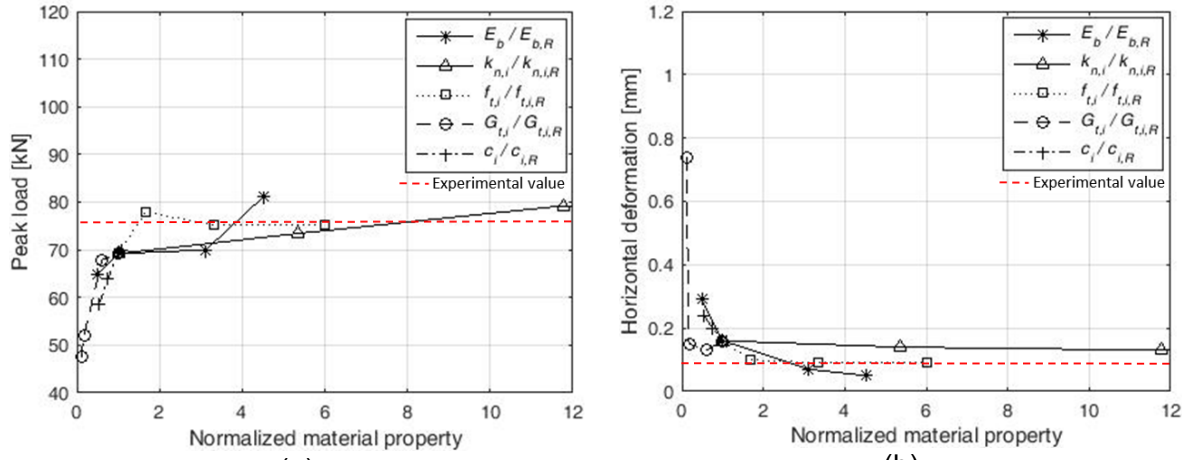

Figure 21. Variation of different material properties within the meso-model. (a) Influence on peak load. (b) Influence on horizontal deformation at the third loading cycle

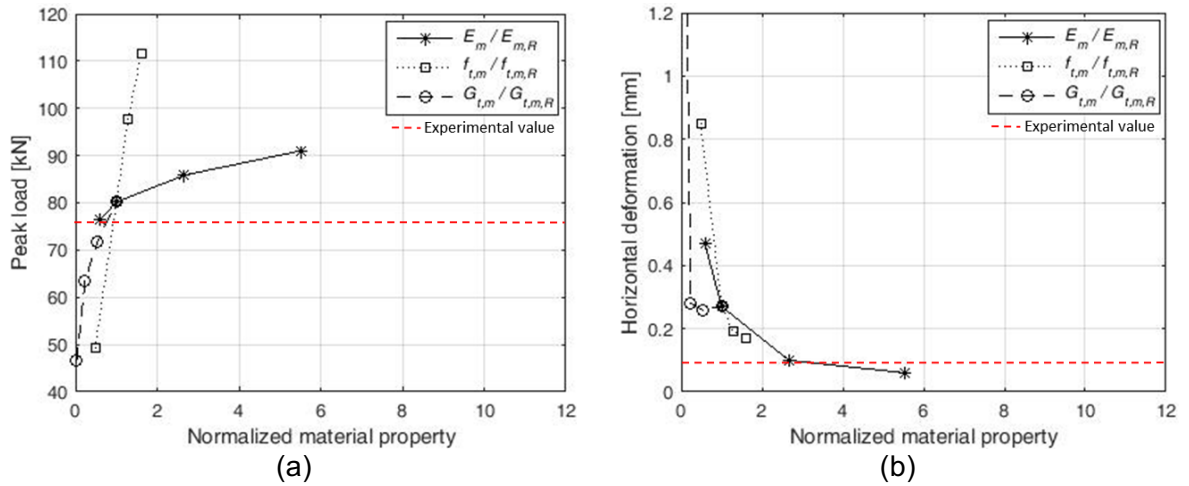

Figure 22. Variation of different material properties within the macro-model. (a) Influence on peak load. (b) Influence on horizontal deformation at the third loading cycle

6. REMARKS AND CONCLUSIONS

This paper presented the implementation and calibration of a discrete cracking meso-model and a continuum smeared cracking macro-model to reproduce the cracking behaviour experimentally observed in a masonry wall subjected to a three point bending test. A sensitivity study was implemented to investigate the effect of material properties variation on both modelling strategies.

For the numerical modelling strategies implemented, it was found that the stiffness properties obtained from laboratory tests on small samples resulted to be too high to represent the masonry element. On the other hand, the numerical strategy implemented to obtain the macro-model material properties from the meso-model properties fulfilled expectations, giving results close to the experimental behaviour of the masonry wall.

After calibration, both numerical modelling approaches presented results in agreement with the experimental data in terms of load capacity, failure mechanism, horizontal deformations and subsequent cracking. However, the meso-model showed higher accuracy and could account for the unrecoverable deformations. The macro-model resulted to be more conservative in terms of predicted crack width.

It is important to consider that the used discrete cracking meso-model requires a wider range of material parameters (some of which require complex lab testing), a higher degree of difficulty in creating the mesh, as well as a longer processing time, in comparison to the continuum smeared cracking macro-model.

The sensitivity analysis showed that some material parameters significantly govern the mechanical behaviour and cracking of the wall. This is an important criterion for adequately choosing the parameters for further models in which cracking is considered, e.g. for settlement-induced cracking analysis. For instance, it was found that tensile fracture energy of the interfaces $G_{t,i}$ as well as the cohesion c_i have an important influence on both the load capacity and crack width in the meso-model. On the other hand, fracture energy of composite masonry $G_{t,m}$ as well as tensile strength $f_{t,m}$ significantly influence the behaviour of the macro-model.

It has to be remarked that the results of the presented sensitivity analysis are valid in relation to the considered parameter value ranges. The latter were determined from limited experimental testing and an extensive study of the relevant literature. This analysis indicated that the intuitive calibration approach which is often applied for masonry models, combining

experimental and literature data, does lead to a good, but not necessarily optimized result. However, optimized calibration of cracking models for a certain masonry type is only possible when an extensive number of large scale experimental data are available.

7. ACKNOWLEDGMENTS

This work was performed within the framework of the GEPATAR project ("GEotechnical and Patrimonial Archives Toolbox for ARchitectural conservation in Belgium" BR/132/A6/GEPATAR), which is financially supported by BRAIN-be, Belspo.

8. REFERENCES

[1] Ovando-Shelley E, Santoyo-Villa E, Pinto M. Geotechnical Considerations for Intervening Historical Constructions. 9th International Conference on Structural Analysis of Historical Constructions SAHC 2014 Mexico City2014.
[2] De Jong MJ. Settlement effects on masonry structures. 10th International Conference on Structural Analysis of Historical Constructions. Leuven, Belgium2016.
[3] Burland JB, Wroth C. Settlement of buildings and associated damage. British Geotechnical Society's Conference on the Settlement of Structures Cambridge 1974. p. 611-54.
[4] Giardina G, Marini A, Hendriks MAN, Rots JG, Rizzardini F. Experimental analysis of a masonry façade subject to tunnelling-induced settlement. Engineering Structures. 2012;45:421-34.
[5] Giardina G, van de Graaf AV, Hendriks MAN, Rots JG, Marini A. Numerical analysis of a masonry façade subject to tunnelling-induced settlements. Engineering Structures. 2013;54:234-47.
[6] Lourenço PB. Computational strategies for masonry structures. Delft: Delft University of Technology; 1996.
[7] Rots JG. Structural Masonry-An Experimental/Numerical Basis for Practical Design Rules. Rotterdam: A.A Balkema; 1997.
[8] Camós C, Molins C, Arnau O. Case study of damage on masonry buildings produced by tunneling induced settlements. International Journal of Architectural Heritage. 2014;8:602-25.
[9] Bloodworth AG. Three-dimensional analysis of tunneling effects on structures to develop design methods. 2002.
[10] Verstrynge E, De Wilder K, Bejarano-Urrego L-E, Voet E, Van Balen K. Advanced techniques for monitoring of settlement induced deformations and crack growth in historical masonry. 10th International Conference on Structural Analysis of Historical Constructions, Leuven, Belgium2016.
[11] Verstrynge E, Wilder KD, Drougkas A, Voet E, Balen KV, Wevers M. Crack monitoring in historical masonry with distributed strain and acoustic emission sensing techniques. Construction & Building Materials. 2018.
[12] European Standard. Methods of test for mortar for masonry Part 11: Determination of flexural and compressive strength of hardened mortar, EN 12390-3,5. Brussels1999.

[13] Federátion Internationale du Béton. . The fib Model Code for Concrete Structures Berlin: Wilhem Ernst und Sohn Verlag für Architektur; 2010.
[14] CEN. EN 1996 Eurocode 6, part 3.6: Design of masonry structures, Mechanical properties of masonry. 2005.
[15] Drougkas A, Roca P, Molins C. Numerical prediction of the behavior, strength and elasticity of masonry in compression. Engineering Structures. 2015;90:15-28.
[16] Lourenço PB, Rots JG. A multi-surface interface model for the analysis of masonry structures. J Struct Eng. 1997;ASCE 123,7:660-8.
[17] TNO. DIANA Finite Element Analysis, User's Manual. In: Manie J, Kikstra WP, editors. Delft TNO DIANA BV; 2016.
[18] Sarhosis V. Optimisation procedure for material parameter identification for masonry constitutive models. Int J Masonry Research and Innovation. 2016;1:48-57.
[19] Sarhosis V, Garrity SW, Sheng Y. Influence of brick-mortar interface on the mechanical behaviour of low strength masonry brickwork lintels. Engineering Structures. 2014;88:1-11.
[20] Giardina G, Hendriks MAN, Rots JG. Sensitivity study on tunnelling induced damage to a masonry façade. Engineering Structures. 2015;89:111-29.
[21] Sarhosis V, Sheng Y. Identification of material parameters for low bond strength masonry. Engineering Structures. 2015;60:100-10.
[22] Van der Pluijm R. Shear behavior of bed joints. In: Hamid A, Harris H, editors. 6th North American Masonry Conference at Drexel University. Philadelphia1993. p. 125-36.
[23] Van der Pluijm R. Non-linear Behaviour of Masonry under Tension.
[24] Reyes E, Casati M, Gálvez J. Cohesive crack model for mixed mode fracture of brick masonry. International Journal of Fracture. 2008;151: 29.
[25] Noort JR. Computational Modelling of Masonry Structures. Delft: Delft University of Technology; 2012.
[26] Verstrynge E, Schueremans L, Van Gemert D. Time-dependent mechanical behavior of lime-mortar masonry. Materials and Structures. 2011;44 (1):29-42.
[27] Verstrynge E, Schueremans L, Van Gemert D, Hendriks MAN. Modelling and analysis of time-dependent behaviour of historical masonry under high stress levels. Engineering Structures. 2011;33:210-7.
[28] Mosalam K, Glascoe L, Bernier J. Mechanical Properties of Unreinforced Brick Masonry, Section1. Department of Energy by Lawrence Livermore National Laboratory; 2009.